Journal of Materials Chemistry A

ROYAL SOCIETY OF CHEMISTRY

PAPER

View Article Online
View Journal

Cite this: DOI: 10.1039/d6ta01212d

Precursor chemistry governing morphology and cation disorder in $AgBiS_2$ solar absorber for photoelectrochemical water splitting

Dayeon Lee,[a] Neul Ha,[b] Jaemin Park,[b] Jisu Jung,[b] Jaewook Lee,[b] Ji Hoon Kim,[b] Sang Uck Lee,[b] Dong-Won Kang,[c] Kaiying Wang[d] and Wooseok Yang *[abe]

$AgBiS_2$ has emerged as a highly promising light-absorbing material for solar energy conversion owing to its direct band gap, strong visible-light absorption, and compatibility with scalable solution-based processing. A particularly intriguing characteristic of $AgBiS_2$ is that its optical absorption coefficient can be markedly enhanced through cation-disorder engineering. Previous studies have demonstrated that solution chemistry can induce cation disorder in $AgBiS_2$; however, it simultaneously governs crystal growth and morphology, including the formation of one-dimensional nanostructures. Despite its importance, the interplay between cation disorder and morphology control has remained poorly understood. Here, we systematically investigate the chemical interactions among thiourea (TU), serving as both a sulfur (S) source and coordinating ligand, metal cations (Ag^+ and Bi^{3+}), and dimethyl sulfoxide (DMSO) as the solvent. Density-functional-theory calculations combined with spectroscopic and structural analyses consistently reveal that both TU and DMSO bind more strongly to Bi^{3+} than to Ag^+. Notably, the comparable binding energies of the TU–Bi and DMSO–Bi complexes impose a thermodynamic constraint on cation disorder. Consequently, increasing the TU concentration suppresses cation disorder, while instead promoting anisotropic crystal growth, leading to the formation of one-dimensional $AgBiS_2$ nanostructures through specific TU–metal coordination. Furthermore, $AgBiS_2$ thin-film photocathodes with controlled nanostructures were fabricated and evaluated for photoelectrochemical (PEC) water splitting, demonstrating how the chemically driven trade-off between cation disorder and morphology directly influences PEC performance.

Received 8th February 2026
Accepted 20th March 2026

DOI: 10.1039/d6ta01212d

rsc.li/materials-a

Introduction

The advancement of solar energy conversion technologies depends critically on the discovery and development of new semiconducting materials that offer efficiency, stability, and environmental sustainability.[1–3] In this context, $AgBiS_2$ has emerged as a promising candidate owing to its suitable direct band gap (1.0–1.4 eV), high absorption coefficient ($\sim 10^5$ cm^{-1} in visible spectral range), and the earth-abundant, non-toxic nature of its constituent elements. Furthermore, $AgBiS_2$ can be synthesized in diverse solution-processing routes (*e.g.*, molecular inks,[4–8] colloidal synthesis[9–11]), offering engineering advantages by enabling simultaneous control over both optical and electrical properties.

Among the characteristics that govern $AgBiS_2$, cation disorder has emerged as a critical factor due to its significant impact on optoelectronic properties. Cation disorder refers to the random distribution of two or more distinct metal cations across the designated crystallographic sites in a multinary compound.[12] This structural deviation occurs when the cations occupy sites that are not strictly dictated by the perfect crystal symmetry, leading to compromised local symmetry and fundamentally altered physical properties. By intentionally introducing cation disorder, the optical, electrical, and thermal properties of a material can be precisely tuned.[13–18] Wang *et al.* demonstrated that cation-disordered $AgBiS_2$ nanocrystals, obtained *via* post heat treatment, exhibited a high absorption coefficient up to 8×10^5 cm^{-1},[9] which enables efficient light harvesting and achieves power conversion efficiencies above 9%. Several subsequent works have explored similar strategies to induce cation disorder, mainly through compositionally controlled nanocrystal synthesis.[10,19]

Nanocrystal-based approaches, however, require multiple processing steps, including synthesis, washing, ligand

[a]Department of Future Energy Engineering (DFEE), Sungkyunkwan University (SKKU), Suwon 16419, Republic of Korea. E-mail: wooseok.yang@skku.edu
[b]School of Chemical Engineering, Sungkyunkwan University, Suwon 16419, Republic of Korea
[c]Department of Energy Systems Engineering, Chung-Ang University, 84 Heukseok-ro, Dongjak-gu, Seoul 06974, Republic of Korea
[d]Department of Microsystems, University of South-Eastern Norway, Horten 3184, Norway
[e]SKKU Institute of Energy Science and Technology (SIEST), Sungkyunkwan University, Suwon 16419, Republic of Korea

exchange, and redispersion, which significantly increase fabrication complexity and cost. Moreover, many studies on nanocrystal-based materials have investigated disorder formation *via* mild post-heat treatment.[12] Such post-heat treatments can induce ligand decomposition or nanoparticle agglomeration, thereby limiting precise control over the degree of cation disorder. In contrast, molecular solution-processed thin-film fabrication offers a simplified, highly scalable route by enabling direct conversion of precursors into a film, thereby overcoming the limitations of nanocrystal-based methods (*e.g.*, extensive surface termination defects at particle boundaries). More importantly, solution-based methods can provide enthalpy- and temperature-driven mechanisms for thermodynamically stable disordered phases ($\Delta G = \Delta H - T\Delta S$), whereas nanocrystal-based methods rely solely on temperature control to achieve disorder stabilization.[4–8] This emerging methodology leverages precursor chemistry to fundamentally influence the local coordination environment of cations. This chemical control enables new thermodynamic pathways for tuning disorder, potentially offering a more precise and scalable alternative to traditional temperature-dependent approaches.[20]

Our group previously demonstrated that cation disorder in $AgBiS_2$ can be effectively engineered using a dithiocarbamate (DTC)-based molecular ink strategy, where the ligand–metal binding energy was identified as the decisive parameter governing cation arrangement.[8] While this work established a clear link between molecular chemistry and optoelectronic properties, it was confined to a DTC ligand and pyridine as the solvent. Consequently, a general framework describing how precursor chemistry governs cation disorder across diverse ligand–metal–solvent systems has yet to be established.[9] Understanding and establishing rational design rules for precursor chemistry is therefore essential, as complex ligand–metal–solvent interactions can influence not only atomic-scale cation disorder but also higher-level structural and optoelectronic characteristics. For instance, chemical interactions fundamentally govern the nucleation and growth kinetics of the $AgBiS_2$ phase. Accordingly, ligand–cation interactions in molecular solutions can also modulate the morphology of final films.[21–28] Given that nanostructuring strategies can significantly affect optical and electrical properties, understanding the dual role of precursor chemistry in both cation disorder engineering and morphology control is crucial. Therefore, a systematic investigation into precursor chemistry is required to establish rational design rules that simultaneously govern cation disorder and morphology control, thereby fully harnessing the optoelectronic potential of $AgBiS_2$.

In this study, we investigate the relationship between chemical interactions, cation disorder, and morphology in $AgBiS_2$ using TU as a S-containing ligand and DMSO as a coordinating solvent. TU–DMSO-based molecular inks are widely employed in solution processing due to their excellent solvating and stabilizing abilities,[4,29–40] and it is well-recognized that the chemical environment of such precursor solutions fundamentally determines the final film's structural quality.[41] However, their impact on the thermodynamic pathways governing cation disorder and morphological evolution has not been fully elucidated. Here, we systematically elucidate how ligand–metal–solvent coordination chemistry dictates precursor speciation, ion-release kinetics, and thin-film growth behavior. Moreover, we investigate how ligand–metal–solvent coordination chemistry, subtly tuned by the TU-to-metal molar ratio (TU/M), governs precursor coordination environments, thin-film growth, and the conditions for enthalpy-driven cation disorder control. Finally, by implementing the engineered $AgBiS_2$ films as photocathodes, we establish a direct link between precursor chemistry, thin-film structure, and PEC performance.

Results and discussion

The precursor solution was prepared by dissolving AgCl and $BiCl_3$ as the sources of Ag and Bi, respectively, together with TU as the S source in DMSO. Precursor inks were then spin-coated onto an Au/Fluorine-doped tin oxide (FTO) substrate and subsequently annealed to form $AgBiS_2$ films. Detailed experimental procedures are provided in the Experimental Section. In this study, the TU/M was varied from 0.5 to 8 to elucidate how molecular coordination chemistry in the precursor ink influences cation disorder and film morphology. The calculated coordination structures of Ag–TU and Bi–TU complexes at their maximum coordination numbers are shown in Fig. 1a and b. In the precursor solution, Ag and Bi exhibit distinct coordination preferences towards the S atom of TU, with a maximum coordination number of 4 and 6, respectively. Representative calculated coordination geometries for Ag–TU (coordination numbers 1–4) and Bi–TU (coordination numbers 1–6) are additionally shown in Fig. S1. To gain a deeper insight into the molecular interactions governing precursor behavior, binding energy calculations were performed for the TU–Ag^+ and TU–Bi^{3+} complexes, complemented by Raman spectroscopy. As shown in Fig. 1c, the binding energy of Bi–TU (approximately −0.5 to −0.2 eV per atom) is significantly larger than that of Ag–TU (about −0.1 eV per atom), indicating a stronger coordination affinity of Bi^{3+} toward TU under identical conditions.

Previous studies have demonstrated that coordination of metal cations to the S atom induces electron delocalization toward the metal center, leading to a weakening of the C=S bond and a red shift of the corresponding vibrational mode.[32] Consistent with previous findings, our calculation results also revealed a red shift in the C=S stretching vibration upon coordination with both Ag^+ and Bi^{3+}, confirming that both cations are coordinated with the C=S moiety in TU (Fig. 1d and e). To experimentally validate these predictions, Raman spectra were collected for solutions containing TU alone as well as TU coordinated with Ag^+ or Bi^{3+}. As shown in Fig. 1f and g, the characteristic C=S stretching mode is clearly observed in the ~745 cm^{-1} region for all solutions. Notably, coordination with either Ag^+ or Bi^{3+} induces a distinct red shift relative to pristine TU, in excellent agreement with the calculated results. The specific wavenumbers for these calculated and experimental peak positions are summarized in Table S1. These results provide direct experimental evidence that metal–TU coordination weakens the C=S bond through coordination-induced

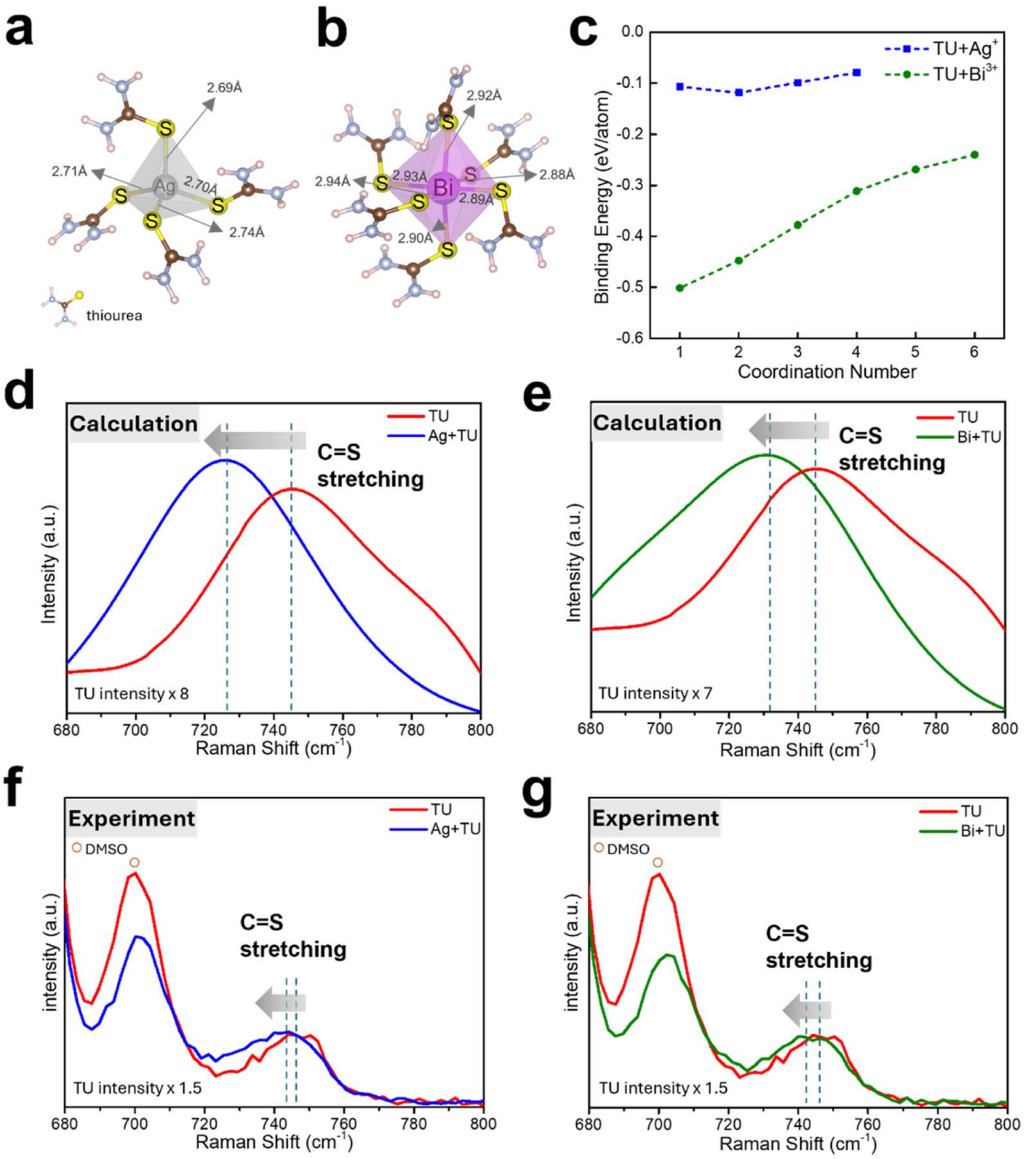

Fig. 1 (a and b) Coordination geometries of metal cations fully saturated with TU ligands: (a) Ag^{+} with four TU ligands (tetrahedral), and (b) Bi^{3+} with six TU ligands (octahedral). (c) Calculated binding energy profile of Ag and Bi cations as a function of coordination number. (d–g) Calculated and experimental liquid Raman spectra comparing the C=S stretching mode of pure TU and TU coordinated with Ag^{+} and Bi^{3+}. Each subplot includes two spectra: TU only and TU + metal cation, illustrating coordination-induced peak shifts.

electronic redistribution, thereby corroborating the coordination-induced electronic interactions in the precursor solutions.

Having established the S-based coordination of TU, we next examined the role of the solvent, DMSO, in metal–ligand interaction. The calculated representative coordination geometries for Ag^{+} and Bi^{3+} with DMSO ligands at the maximum coordination numbers are illustrated in Fig. S2a and b, which shows the strong solvation capacity of DMSO. This effective solvation plays a key role in modulating the coordination behavior of TU toward Ag^{+} and Bi^{3+}, thereby altering respective coordination mechanisms. Solution-phase Raman Spectroscopy offers direct insight into the coordination modes of Ag^{+} and Bi^{3+} with TU in DMSO, reflecting their interaction pathways in the actual chemical environment (Fig. 2a–d). In the *n*TU(M), *n* denotes the TU/M when both Ag^{+} and Bi^{3+} are present at 0.2 M each (*i.e.*, a total metal concentration of 0.4 M). When only a single metal cation is present, the notation is written as nTU(Ag) or nTU(Bi); in these cases, the effective TU-to-metal molar ratio becomes 2*n*, as the metal concentration remains fixed at 0.2 M throughout this study.

Under the 1TU condition, the C=S stretching peak of TU exhibits a greater red shift in the presence of Ag^{+} than in the presence of Bi^{3+}, indicating a stronger binding interaction between Ag^{+} and TU. As the molar ratio increases, this shift gradually diminishes. In contrast, under Bi^{3+} conditions, the C=S peak does not shift at 1TU but progressively red shifts with increasing TU concentration, eventually overlapping with the

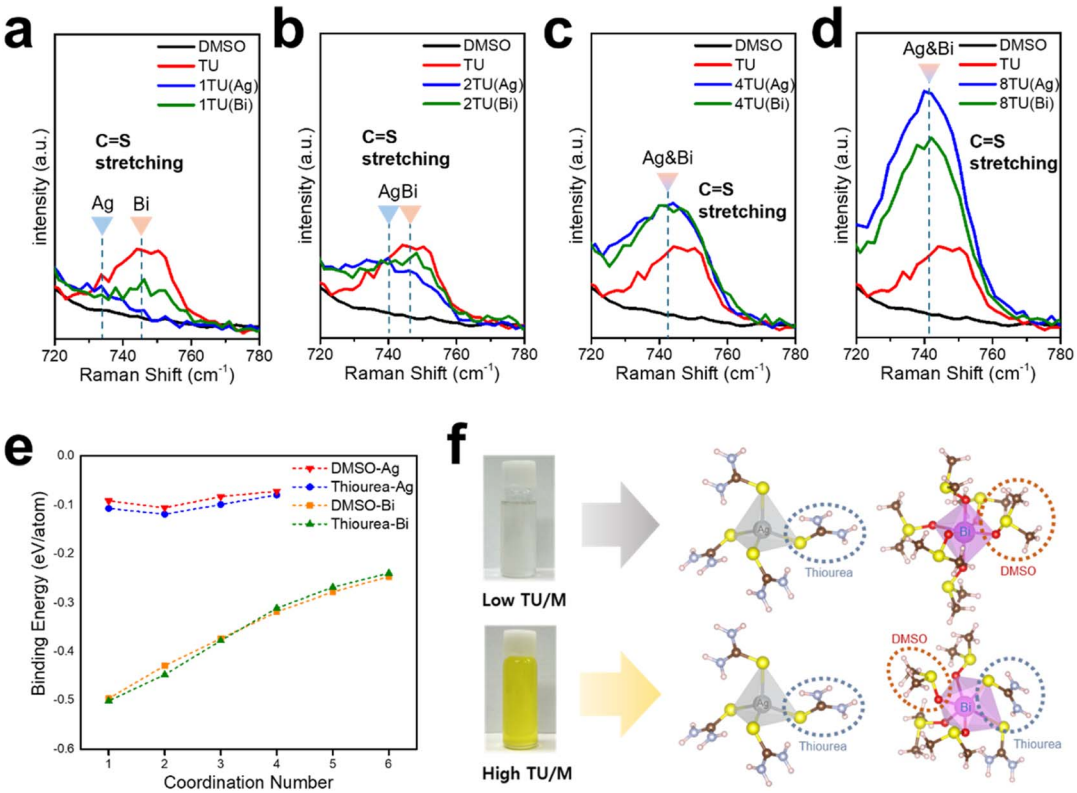

Fig. 2 The *n*TU(M) notation is defined in the main text. (a–d) Raman spectra of TU solution with Ag^+ or Bi^{3+} at *n*TU(M) conditions ($n = 1, 2, 4, 8$). The dashed lines and arrows indicate the C=S stretching peak positions in the *n*TU(Ag) and *n*TU(Bi) conditions. (e) Calculated binding energy profile of Ag and Bi cations with TU and DMSO as a function of coordination number. (f) Schematic illustration of coordination structures in Ag–Bi–TU–DMSO molecular inks with (top) low and (bottom) high TU/M ratios. The color of the solution and the metal–ligand coordination environment vary depending on the TU concentration.

C=S peak observed under Ag^+ conditions. The precise peak positions for these concentration-dependent shifts are systematically compiled in Table S2. A similar trend is observed in the C–N stretching region, where increasing TU concentration leads to progressive red shifts in the C–N vibration of TU (Fig. S3). This behavior reflects the electron redistribution across the TU backbone upon metal coordination and is consistent with previous reports demonstrating the sensitivity of the C–N bond to metal coordination.[32]

To further clarify this behavior, binding energy calculations were performed for Ag^+ and Bi^{3+} with TU and DMSO (Fig. 2e). The results show that Ag^+ preferentially binds to TU than to DMSO across all coordination numbers considered. In contrast, Bi^{3+} exhibits a coordination-number-dependent preference: TU coordination is favored at lower coordination numbers (*e.g.*, 1–3), whereas DMSO binding becomes increasingly favorable at higher coordination numbers (*e.g.*, 4–6). It should be noted that although thermal effects at finite temperatures may influence the absolute binding strengths, the relative preference between DMSO and TU coordination is expected to remain unchanged. These results suggest that the C=S peak shifts observed in the Raman spectra with varying TU concentration originate from the dynamic competition between TU and DMSO for metal coordination.

Taken together, the overall coordination equilibria can be represented as follows, illustrating the ligand exchange process between DMSO and TU around the Bi^{3+} center:

$$Bi(DMSO)_n + TU \rightleftharpoons Bi(DMSO)_{n-1}(TU) + DMSO \quad (1)$$

$$Bi(DMSO)_{6-x}(TU)_x \ (x \approx 2\text{–}3) \quad (2)$$

Eqn (1) represents the initial step of the ligand exchange reaction, where one DMSO molecule coordinated to the Bi^{3+} center is substituted by one TU molecule. This equilibrium drives the formation of mixed-ligand complexes. Eqn (2) describes the final, stable mixed-ligand complex formed when TU concentration is sufficiently high. Here, Bi^{3+} typically adopts a stable coordination sphere containing a fixed number of TU molecules (where x is typically 2 to 3) along with the remaining DMSO molecules, resulting in a combination complex. Consistent with this coordination behavior, the Bi–S stretching peaks observed in both the calculated and experimental Raman spectra (Fig. S2c and d) indicate the gradual formation of Bi–TU coordination as the TU concentration increases. The Bi–S stretching peaks undergo a red shift, which can be attributed to the progressive weakening of individual Bi–S bonds as TU gradually replaces coordinated DMSO molecules. This ligand substitution leads to bond lengthening and increased electron

donation from multiple TU ligands, resulting in softer Bi–S interactions.

Combining Raman spectroscopy with theoretical validation, we conclude that Ag^+ preferentially coordinates with TU at low TU concentrations in DMSO solvent, while Bi^{3+} primarily favors solvation by DMSO and incorporates TU only at higher TU concentrations. This distinction in coordination preference is clearly illustrated by the structural models in Fig. 2f, which highlight the contrasting ligand environments surrounding each metal center. Notably, the transition from a purely DMSO-coordinated Bi^{3+} sphere to a TU-containing mixed-ligand complex is accompanied by a pronounced change in the optical appearance of the solution. At high TU/M ratios, the solution appears more intensely yellow, consistent with the formation of Bi–TU complexes. This color change is likely attributed to coordination-induced electronic interactions—specifically, electron donation from S atoms in TU to the Bi^{3+} center—which modify the visible-light absorption characteristics of the solution. As shown in Fig. S4a, the solution containing Bi and TU in DMSO exhibits a distinct yellow coloration, which intensifies with increasing TU concentration at a fixed Bi content, indicating enhanced Bi–TU coordination. To further utilize this optical transition as a probe for competitive binding, we compared the 1TU(Bi) (TU 0.4 M, Bi 0.2 M) solution with the 2TU(Ag + Bi) (TU 0.8 M, Ag 0.2 M, Bi 0.2 M) solution in Fig. S4b. If TU coordinated indiscriminately to Ag^+ and Bi^{3+}, the amount of TU bound to Bi^{3+} in 2TU(Ag + Bi) would be comparable to that in the 1TU(Bi), given the identical Bi^{3+} concentration and overall TU/M ratio. Under such conditions, both solutions would be expected to exhibit similar yellow color intensity. However, the 1TU(Bi) solution displays a more pronounced yellow hue than 2TU(Ag + Bi) (Fig. S4b). This observation indicates that, in the presence of Ag^+, TU preferentially coordinates with Ag^+, thereby suppressing Bi–TU complexation through competitive binding.

Building on these solution-phase insights, we examined how coordination preferences influence the morphological and compositional evolution of the resulting $AgBiS_2$ films. Energy-dispersive X-ray spectroscopy (EDS) and scanning electron microscopy (SEM) were employed to elucidate the composition and microstructure of the $AgBiS_2$ as a function of TU/M molar ratios. As shown in Fig. 3a, increasing the TU/M molar ratio from 0.5 to 8 leads to a gradual shift in the Ag/Bi ratio in the resulting thin films, from Ag-rich to marginally Bi-rich composition. This behavior arises from the preferential coordination of Ag^+ with TU over Bi^{3+} in DMSO. At low TU/M ratios, Ag^+ more readily coordinates with TU compared to Bi^{3+}, resulting in dominant Ag–TU complexes, while Bi^{3+} remains largely coordinated with DMSO solvent molecules. As the TU concentration increases, Bi^{3+} increasingly engages in coordination with TU, thereby altering the relative availability of Ag and Bi species during film formation and ultimately shifting the film composition.

SEM images of $AgBiS_2$ films with different TU/M ratios reveal that the films predominantly exhibit nanorod-like morphologies except at a low TU/M ratio of 0.5 (Fig. 3b–f). As the TU/M ratio increases, both the diameter and length of the nanorods predominantly increase, indicating enhanced anisotropic growth. The growth mechanism underlying these observations, as illustrated in Fig. 3g, is fundamentally governed by the interplay between thermodynamic phase evolution and kinetic growth control. According to previous thermal gravimetric analyzer (TGA) analysis, the thermal decomposition temperature of the Ag–TU complex is approximately 235 °C, whereas that of the Bi–TU complex is around 218 °C.[30] Consequently, during film formation under annealing at 280 °C, the Bi–TU complex decomposes before the Ag–TU complex, providing the thermodynamic driving force for the earlier release of Bi^{3+} and S species. This early release initiates the pre-nucleation crystallization process, predominantly forming the Bi_2S_3 framework. It should be noted that Bi_2S_3 is well known to preferentially form one-dimensional nanostructures due to its intrinsically anisotropic crystal structure.[42–44] Upon continued heating, the Ag–TU complex subsequently decomposes, releasing Ag^+ ions that diffuse into pre-formed Bi_2S_3 framework. This sequential process leads to the formation of $AgBiS_2$ *via* a gradual cation incorporation process, resembling a partial cation exchange mechanism that ultimately completes the transformation into the ternary phase.[43] Importantly, the structural integrity during this transformation depends on the physical dimensions of the precursor. In this study, the precursor-derived structures exhibit relatively large diameters, which are significantly greater than the typical width of the non-equilibrium reaction zone (4–5 nm) formed during solid-state diffusion.[43] This substantial dimensional margin ensures kinetic stability by effectively preventing morphological collapse during the transformation, thereby enabling the preservation of the nanostructure's original shape throughout the annealing process. In contrast, at a low TU/M ratio (TU/M = 0.5), the diameter of the nanorods becomes comparable to or smaller than the reaction zone width, leading to structural instability and collapse during film formation and resulting in the formation of non-rod-like morphologies.

This growth behavior is further influenced by the molar ratio of TU/M, which regulates both the coordination behavior and diffusion kinetics of Ag^+ and Bi^{3+} species during film formation. At low TU/M ratios, the high concentration of Ag–TU complex promotes early and rapid diffusion of Ag^+ into the initially formed Bi_2S_3 nanorods. This accelerated Ag^+ incorporation triggers a premature kinetic phase conversion from Bi_2S_3 to $AgBiS_2$, which terminates the growth process before the templates can fully develop, resulting in the formation of shorter nanorods. In contrast, at high TU/M ratios, TU more effectively coordinates with metal cations, forming a balanced population of Ag–TU and Bi–TU complexes. This coordination environment suppresses premature Ag^+ release and allows Bi_2S_3 nanorods undergo further anisotropic growth before Ag^+ insertion. Consequently, $AgBiS_2$ forms through gradual cation incorporation along well-developed Bi_2S_3 templates, resulting in longer nanorods. In addition, the increased TU content enhances the solubility and availability of Ag, Bi, and S species in the precursor solution, further facilitating the growth through enhanced species transport. Overall, the final nanorod dimensions are determined by both the thermodynamic sequence of phase formation, directed by precursor

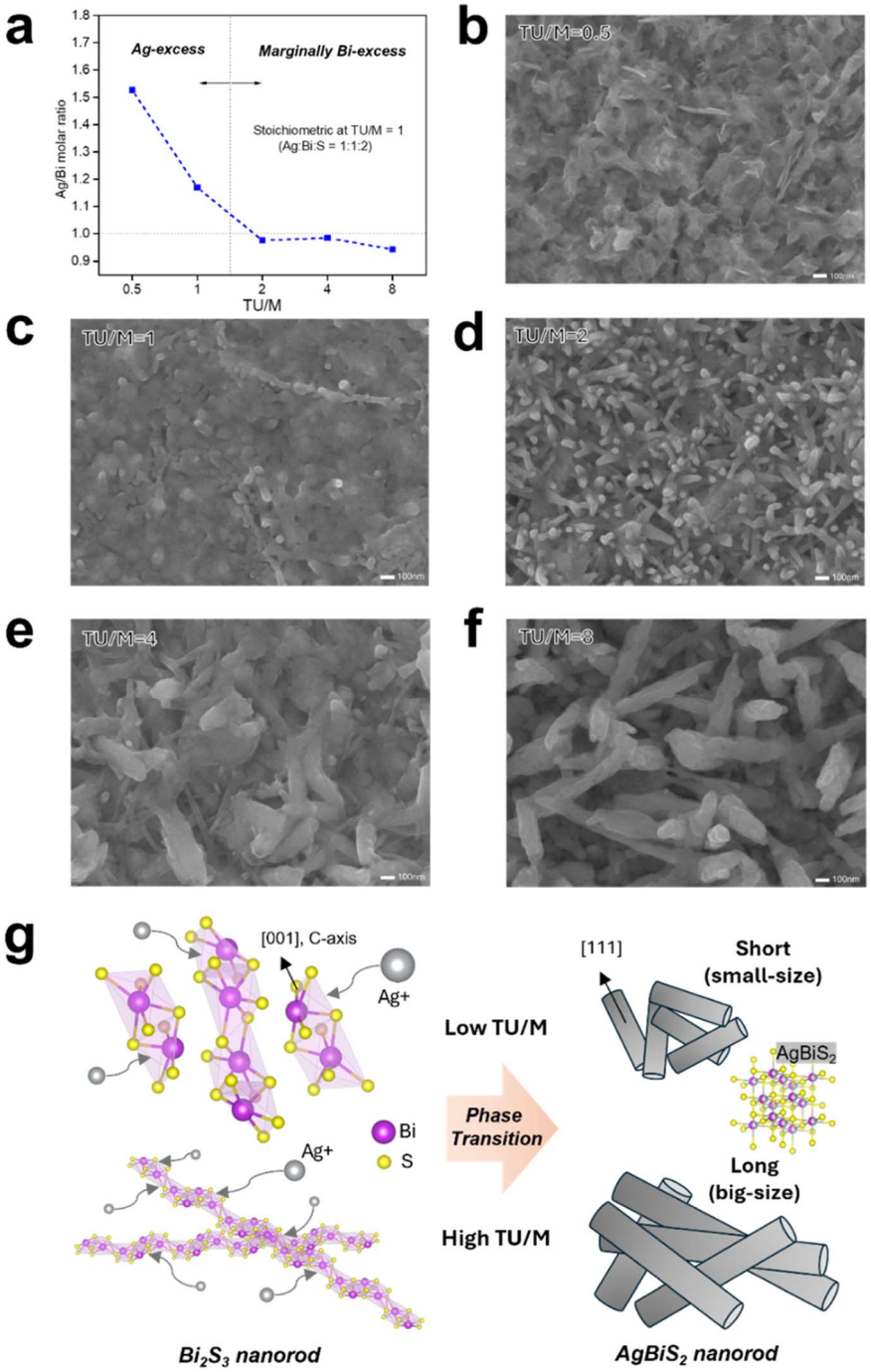

Fig. 3 (a) Ag/Bi molar ratio in $AgBiS_2$ thin films as a function of TU/M molar ratio (0.5, 1, 2, 4, 8) in the precursor solution. (b–f) Surface SEM images of $AgBiS_2$ thin films synthesized from various TU/M molar ratios in Ag–Bi–TU–DMSO molecular inks (all films were fabricated at 3000 rpm with 4 coating cycles). (g) Schematic illustration of the proposed growth mechanism of $AgBiS_2$ nanorods. (Dimensions not to scale).

decomposition, and the kinetic modulation of diffusion rates and structural margins. Although direct *in situ* observation of the precursor-to-crystal transition remains technically challenging under high-temperature annealing conditions, the consistent alignment between our DFT calculations, Raman spectroscopy, and kinetic modeling provides a rigorous analytical framework that sufficiently validates the proposed mechanism. By systematically linking the initial coordination environment to the final nanostructural evolution, we confirm that the observed anisotropic growth is a causative result rooted in fundamental chemical principles rather than mere empirical correlation.

X-ray diffraction (XRD) pattern was investigated to verify phase formation and lattice evolution in $AgBiS_2$ thin films. Fig. S5 confirms the formation of phase-pure $AgBiS_2$ across all TU/M ratios, while Fig. 4a–c reveals a non-monotonic shift in

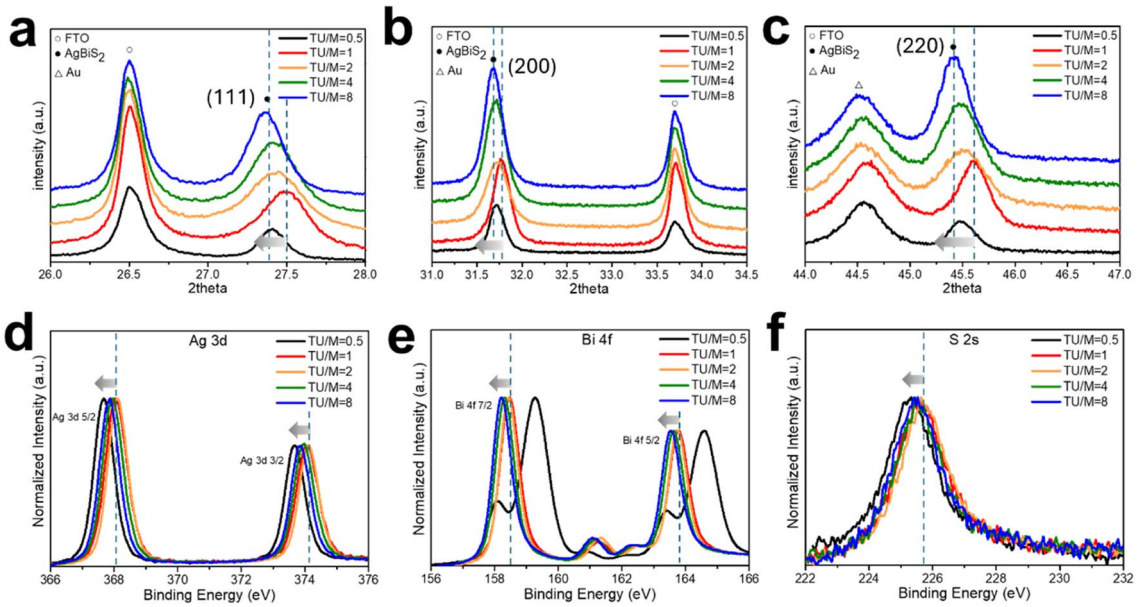

Fig. 4 (a–c) XRD patterns and (d–f) XPS spectra demonstrating the influence of different TU/M ratios of precursor solution on $AgBiS_2$ thin films (fabricated at 3000 rpm with 6 coating cycles) deposited on Au/FTO substrates and annealed at 200 °C.

the diffraction peak positions under varying TU/M molar ratios. When the TU/M ratio increases from 0.5 to 1, the primary diffraction peaks shift toward higher 2θ angles, suggesting a decrease in the lattice constant. It is primarily attributed to compositional effects. Considering the difference in ionic radii between Ag^+ (1.15 Å) and Bi^{3+} (1.03 Å), the excess incorporation of the larger Ag^+ ions likely leads to lattice expansion, whereas at higher TU/M ratios, Bi^{3+} substitution results in a reduced lattice constant. Such compositional asymmetry at low TU/M gives rise to a difference in lattice constants. On the other hand, beyond TU/M = 1, the continued shift of the diffraction peaks toward lower 2θ angles implies an expansion of the lattice that is no longer explained by ionic composition alone. This structural evolution is consistent with morphological changes in the nanorods described earlier. At higher TU/M ratios, the formation of sufficient Ag–TU and Bi–TU complexes modulates the release kinetics of metal ions, enabling more complete growth of the Bi_2S_3 template before Ag^+ incorporation. This results in longer and more fully developed $AgBiS_2$ nanorods. Such dimensional growth may promote partial relaxation of residual lattice strain. Consistent with this interpretation, Sharma *et al.* reported that in Ni_3TeO_6 nanostructures, an increase in particle size leads to the reduction of lattice strain, which is reflected by a shift of XRD peaks toward lower 2θ angles.[45] A similar trend is observed in this study, where the size of $AgBiS_2$ nanorods gradually increases with TU/M ratio, reducing grain boundary density and alleviating internal lattice strain.

The X-ray photoelectron spectroscopy (XPS) data shown in Fig. 4d–f further support this structural evolution, revealing a distinct non-monotonic trend in core-level binding energies. From TU/M = 0.5 to 1, the binding energies of the Ag 3d, Bi 4f, and S 2s core levels exhibit a slight increase. However, from TU/M = 1 to 8, all core levels exhibit a simultaneous shift toward lower binding energies. This collective behavior can be rationalized by the expansion of the lattice, which increases the average interatomic distance and consequently reduces the Madelung potential-the cumulative long-range Coulombic interaction felt by core-level electrons at their respective lattice sites.[46] Since this electrostatic potential is inversely proportional to the lattice distance, the overall weakening of these interactions leads to a downward shift of the entire core-level energy spectrum. This uniform shift is further evidenced by the constant energy difference between the Ag 3d and S 2s peaks (142.40 eV), confirming that the shift results from global structural relaxation rather than localized redox changes. Such a binding energy shift is consistent with the trend reported by Sharma *et al.* as well,[45] where the relief of lattice strain during structural evolution leads to electronic stabilization, further supporting the correlation between our observed lattice expansion and the downward shift in core-level energies.

Taken together, the XRD (Fig. 4a–c) and XPS (Fig. 4d–f) analyses reveal that morphology-driven strain relaxation, in conjunction with compositional effects, plays a key role in governing the structural and electronic properties of $AgBiS_2$ thin films. At low TU/M ratios, excess Ag^+ content appears to induce lattice expansion and higher binding energies due to ionic size mismatch and compositional imbalance. As the TU/M ratio increases beyond 1, the development of longer and more continuous nanorods facilitates partial strain relaxation, which is reflected in both lattice expansion and a shift toward lower binding energies. These observations highlight the dynamic between precursor chemistry, crystal growth behavior, and internal lattice strain factors that may also impact other key properties of the films, as discussed in subsequent sections.

Beyond morphological and structural characterization, we further examine whether the molecular precursor chemistry

explored in earlier sections governs cation disorder in the final $AgBiS_2$ films. The degree of cation disorder is theoretically defined by the order parameter $S = 2(P_A^A - 0.5)$, where P_A^A represents the probability of a cation occupying its designated lattice site, with $S = 1$ and $S = 0$ denoting perfectly ordered and fully disordered states, respectively.[12] However, since determining an absolute numerical value for S in experimental thin films is inherently challenging due to complex local configurations, the terms 'order' and 'disorder' in this study refer to the relative structural states of the cation arrangement rather than absolute quantities. To this end, we adopt a thermodynamic framework based on regular solution theory, which allows us to evaluate the energetic driving force for disorder formation.[8] The interaction parameter χ is defined as follows:

$$\chi = \frac{z}{kT}(2\varepsilon_{AB} - \varepsilon_{AA} - \varepsilon_{BB}) \quad (3)$$

where A refers to the Ag–ligand complex (either Ag–TU or Ag–DMSO) and B refers to the Bi–ligand complex (either Bi–TU or Bi–DMSO). The term ε_{AB} represents the interaction energy between the Ag–ligand and Bi–ligand complexes, while ε_{AA} and ε_{BB} are the interaction energies within the Ag–ligand and Bi–ligand complexes, respectively. Here, z denotes the coordination number of the A and B complexes, reflecting the number of nearest–neighbor interactions considered in the model, while k and T are Boltzmann's constant and the temperature, respectively. The value of χ quantifies the energetic contrast between Ag–ligand/Bi–ligand interactions and their respective self-interactions. When the interaction energy ε_{AB} between the Ag–ligand and Bi–ligand complexes is close to the average of ε_{AA} and ε_{BB}, the value of χ becomes small ($\chi \approx 0$), thereby favoring a homogeneous, cation-disordered phase.

At low TU/M ratios, 6 DMSO primarily coordinates with Bi, while 4 TU coordinates with Ag. This results in different coordination environments for Ag and Bi, namely $[Ag(TU)_4]^+$ and $[Bi(DMSO)_6]^{3+}$ complexes. Owing to the large structural difference between the Ag and Bi complexes, the interaction energy ε_{AB} is expected to deviate significantly from the average of ε_{AA} and ε_{BB}. This asymmetry leads to a relatively large value of χ, which directly translates to a high enthalpy of mixing (ΔH_{mix}), thus thermodynamically favors cation segregation. At high TU/M ratios, TU not only coordinates with Ag, but also substitutes DMSO in the Bi–DMSO complex to form mixed-ligand complexes ($Bi(DMSO)_{6-x}(TU)_x$ ($x \approx 2$–3)). Despite this ligand substitution, the structural similarity between the resulting Ag^+ and Bi^{3+} ligand complexes remains low, primarily due to substantial differences in coordination number and ligand environment. This persistent structural mismatch between the Ag– and Bi–ligand complexes imposes a strong thermodynamic penalty on hetero-cation mixing, thereby suppressing the formation of a cation-disordered phase in the resulting $AgBiS_2$ films. Consequently, the enthalpy-driven cation disorder tuning strategy previously employed by our group-which focused on stabilizing the disordered phase by minimizing the enthalpy of mixing-is not effective in the present TU–DMSO system. Instead, the intrinsic structural incompatibility between the Ag^+ and Bi^{3+} precursor complexes increases the enthalpy penalty, thereby destabilizing the disordered state and fundamentally suppressing cation disorder.

Furthermore, the thermodynamic principles established here suggest that the correlation between precursor coordination chemistry and cation disorder is not confined to the TU–DMSO system but serves as a more universal framework governed by the competitive coordination of solvents and ligands. For instance, in systems using non-coordinating solvents such as pyridine (*e.g.*, the DTC/pyridine system), metal cations are fully coordinated solely by ligands. This leads to high structural similarity between the Ag and Bi complexes, thereby minimizing the mixing enthalpy and providing a driving force for cation disorder.[7] In contrast, our findings demonstrate that using a coordinating solvent like DMSO, combined with the distinct coordination numbers of Ag and Bi, maintains structural dissimilarity and thermodynamically suppresses disorder. These guidelines provide a theoretical foundation for predicting and designing cation arrangements in various multicomponent chalcogenide thin films by strategically selecting precursor solvents and ligands.

This thermodynamic interpretation is consistent with the XRD and XPS results. In previously reported cases of cation disorder in $AgBiS_2$, XRD peaks shift to the higher angles due to lattice contraction; similarly, XPS peaks for Ag 3d and Bi 4f typically shift to lower binding energies.[12] In contrast, our TU–DMSO system exhibits an opposite XRD trend (Fig. 4a–c), with diffraction peaks shifting toward lower 2θ angles as the TU/M ratio increases from 1 to 8. Consistent with this interpretation, the XPS spectra display a collective and uniform shift of all constituent elements–Ag, Bi, and S–to lower binding energies (Fig. 4d–f). Such synchronized behavior confirms that these changes originate from global strain relaxation rather than localized atomic redistribution. Given the bulk-sensitive nature of X-ray diffraction, the observed cation disorder suppression and strain relaxation represent the crystallographic state of the entire $AgBiS_2$ absorber rather than a localized surface phenomenon. This bulk-centered structural evolution is particularly significant considering our device architecture ($AgBiS_2$/CdS/TiO_2/Pt), where the $AgBiS_2$ layer is encapsulated by multiple functional layers. Since the absorber is not in direct contact with the electrolyte, its bulk crystallographic quality—defined by the relative degree of cation disorder—is expected to be the primary factor governing the eventual PEC response, rather than the extreme surface states. Collectively, these results demonstrate that structural refinement through strain relaxation, accompanied by nanorod growth, dominates the evolution of the $AgBiS_2$ films in the TU–DMSO system.

To evaluate the PEC performance, a multilayer photocathode with the configuration of FTO/Au/$AgBiS_2$/TiO_2 (1 nm)/CdS/TiO_2/Pt was fabricated. A detailed device structure, including thickness for each layer, can be found in Fig. S6. The thickness of the $AgBiS_2$ layer varies with the precursors. For systematic comparison, $AgBiS_2$ films prepared at TU/M = 1 and 8 were selected, as these conditions exhibit the most distinct differences in nanostructural dimensions and lattice parameters. To ensure optimized interfacial charge extraction, a 1 nm-thick TiO_2 passivation layer (15 ALD cycles) was deposited, followed

by a UV-ozone treatment to improve surface hydrophilicity for the subsequent CdS buffer layer growth (CBD at 56.5 °C for 11.5 min). The electron transport layer and co-catalyst were then integrated *via* 750 cycles of TiO_2 ALD and Pt ion-sputtering (10 mA, 60 s), respectively. These specific deposition parameters were precisely controlled to achieve high structural reproducibility and efficient PEC performance. The optimization process for the $AgBiS_2$ deposition conditions and the TiO_2 electron transport layer (ETL) thickness is shown in Fig. S7 and S8. Detailed experimental procedures are provided in the Experimental Section. The PEC performance was evaluated by linear sweep voltammetry (LSV) measurements conducted in a three-electrode configuration under simulated AM 1.5 G solar illumination, using a K–Pi buffer solution at neutral pH as the electrolyte. To ensure the measured photocurrents represent the intrinsic PEC response of the photocathodes, all measurements were conducted after N_2 purging to eliminate the effects of dissolved oxygen, the impact of which is shown in Fig. S9. The introduction of an ultrathin (1 nm) TiO_2 interlayer between $AgBiS_2$ and CdS proved to be critical for enhancing the overall PEC performance.[7] Acting as both a chemical and physical passivation layer, this TiO_2 film facilitates efficient electron tunneling from $AgBiS_2$ to CdS, thereby suppressing interfacial charge recombination and promoting effective charge separation.[47] This type of interface engineering is a well-established approach for suppressing surface-state-mediated losses and enhancing the contribution of bulk properties to the overall device performance.[48,49] This passivation effect also prevents Cd interdiffusion into the $AgBiS_2$ layer during the CBD of CdS, preserving the compositional and structural integrity of the photoabsorber. By simultaneously blocking defect-mediated recombination and maintaining a clean, energetically favorable interface for electron transfer, the TiO_2 interlayer contributes significantly to both improved photocurrent response and long-term operational stability of the photocathode.

Fig. 5a shows the LSV results of the photocathodes prepared using different $AgBiS_2$ films with different TU/M ratios. At 0 V *versus* the reversible hydrogen electrode (RHE), the TU/M = 8 photocathode exhibited a photocurrent density of approximately 1 mA cm^{-2}, nearly 1.25 times higher than that of the TU/M = 1 counterpart (0.8 mA cm^{-2}). In addition, a noticeable decrease in dark current was observed, indicating suppressed interfacial recombination and more efficient charge extraction under illumination. This enhancement suggests that the change in precursor chemistry and the resulting modification of the $AgBiS_2$ film structure strongly influenced the PEC activity. To elucidate the origin of this improved performance, the optical and electronic properties of the two films were further investigated. Fig. 5b and c show the optical properties of $AgBiS_2$ films prepared with different TU/M ratios. Tauc analysis based on the Kubelka–Munk function (Fig. 5c) reveals a clear widening of the optical bandgap from 1.12 eV (TU/M = 1) to 1.18 eV (TU/M = 8). Band alignment analysis (Fig. S10) indicates that this bandgap widening originates from an upward shift of the conduction band minimum (CBM), while the valence band maximum (VBM) remains nearly unchanged. This behavior is consistent with the XPS results, where a systematic downward shift of the Bi 4f binding energy is observed at higher TU/M ratios. According to Ju *et al.*, the CBM is dominantly contributed by Bi 6p orbitals, and this shift suggests a reconfiguration of these orbitals as the Bi–S framework evolves.[50] In contrast, while downward shifts are also observed in the Ag 3d and S 2s core levels, they result in a negligible net influence on the VBM. This suggests that the Ag–S hybridization, which forms the VBM, provides a relatively stable electronic baseline that resists significant energy shifts. Beyond electronic effects, structural evolution plays a key role in the observed bandgap widening. Increasing the TU/M ratio promotes the formation of more extended Bi–S frameworks, which serve as the initial structural template for nanorod growth. The subsequent Ag insertion into this expanded framework leads to larger grain sizes and reduced lattice distortion. This structural refinement modifies the local crystal field and dictates the upward shift of the Bi 6p-derived CBM, while the Ag–S based VBM is pinned by the stable coordination environment. Together, the expansion of the Bi–S framework and subsequent strain relaxation provide a structural origin for the bandgap increase observed in both optical and electronic analyses.

While $AgBiS_2$ is generally valued for its intrinsically narrow bandgap, which enables long-range solar absorption, the moderate bandgap widening observed in the TU/M = 8 film provides a distinct interfacial advantage. The work function was determined by subtracting the secondary electron cutoff (SECO) value from the photon energy (He I, $h\nu$ = 21.22 eV), while the VBM was obtained through linear extrapolation of the Fermi edge (Fig. S11). As shown in Fig. 5d and e, this potential-induced electronic restructuring causes an upward shift of the CBM, resulting in a more favorable alignment with the CdS and TiO_2 layers. Although a wider bandgap may slightly reduce light absorption, the resulting higher CBM position enhances the driving force for electron injection and suppresses interfacial recombination. Furthermore, the smaller conduction band cliff between $AgBiS_2$ and CdS under the TU/M = 8 condition allows the ultrathin TiO_2 interlayer to function more effectively as an electronic bridge. With its conduction band edge located between those of $AgBiS_2$ and CdS, TiO_2 mitigates the residual energy discontinuity and facilitates smooth electron tunneling across the junction. This energetically moderate interface contributes to efficient charge extraction and improved PEC performance.

Building on the favorable band alignment discussed above, XPS depth profiling (Fig. 5f, g and S12) provides further insight into the interfacial structure and chemical uniformity of the photocathodes. While band alignment defines the energetic driving force for charge transport, the depth profiles reveal how effectively these pathways are physically connected across the multilayer architecture. Both samples exhibit the expected $AgBiS_2$/CdS/TiO_2 configuration; however, the TU/M = 8 film shows more gradually varying elemental distributions across the interfaces, indicative of conformal CdS and TiO_2 coatings on the $AgBiS_2$ nanorods. This extended interfacial overlap implies a larger and more continuous contact area, which is beneficial for efficient charge extraction and suppression of interfacial recombination.

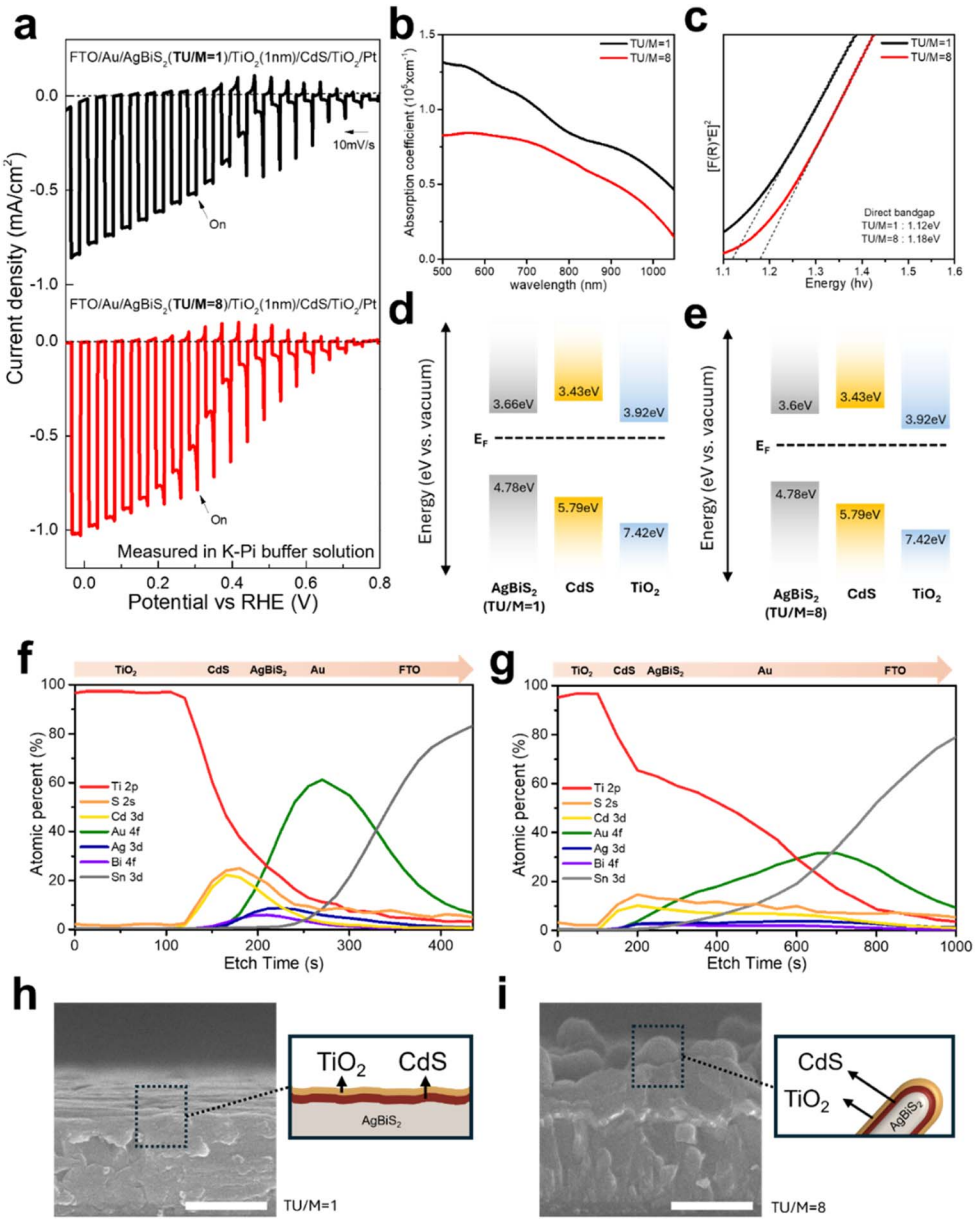

Fig. 5 (a) Chopped-light LSV curves of FTO/Au/$AgBiS_2$/TiO_2(1 nm)/CdS/TiO_2/Pt under AM 1.5 G simulated sunlight. Measurements were performed in 0.5 M K–Pi buffer (pH 7.02) with a scan rate of 10 mV s^{-1} in the cathodic direction. The light was chopped at 2 s intervals. (b) Absorption coefficient and (c) Tauc plot under varying the TU/M ratio. (d and e) Fermi-level–aligned band diagram of the $AgBiS_2$ photocathode for TU/M = 1 (d), TU/M = 8 (e). CBM (top) and VBM (bottom) energies are referenced to vacuum and obtained from UPS combined with optical band gaps. (f and g) XPS depth profile of PEC device fabricated from $AgBiS_2$ film: (f) TU/M = 1 film (g) TU/M = 8 film. (h and i) Cross-sectional SEM images of $AgBiS_2$ photocathode and schematic illustrations of the layer structures: (h) the TU/M = 1 film and (i) the TU/M = 8 film. The 1 nm TiO_2 interlayer is omitted in the schematic for clarity. The scale bar is 500 nm.

The morphological origin of these interfacial characteristics is further confirmed by cross-sectional SEM images (Fig. 5h and i), which clearly reveal the well-developed $AgBiS_2$ nanorod architecture formed at high TU/M ratios. Beyond improving interfacial conformity and layer uniformity, this nanorod network promotes grain growth, thereby reducing grain-boundary density and associated trap states that typically facilitate non-radiative recombination. Consequently, improved carrier separation and transport are achieved. Furthermore, while PEC performance is inherently sensitive to surface states, the $AgBiS_2$ absorber in our configuration is fully encapsulated by multiple protective layers and does not come into direct contact with the electrolyte. Consequently, the overall PEC response is primarily governed by the physical state of the bulk film rather than the extreme surface conditions of the absorber. Overall, the enhanced PEC performance of the TU/M = 8 photocathode arises from the synergistic effects of optimized band alignment, coherent interfacial structure, and refined nanostructural morphology, all enabled through precursor-controlled compositional and structural engineering. It

should be noted, however, regarding the stability of the $AgBiS_2$ photocathode, we observed a performance decline during initial operation, which can be attributed to several complex pathways common in metal chalcogenide systems. The degradation of PEC devices typically involves chemical leaching of elements, photocorrosion, interface charge accumulation, and physical delamination.[53] Given the complexity of these interrelated factors—especially within a multi-layered interface—a precise real-time decoupling of each degradation mode presents a significant experimental challenge. We expect that future studies focusing on advanced interfacial passivation and robust protective layer engineering will address these stability challenges. Moreover, considering that the application of $AgBiS_2$ in PEC water splitting is in its nascent stage, with the initial benchmark reported only recently, our findings reflect the early-stage characteristics of this material system.[7] While the current photocurrent density and stability have not yet reached the levels of state-of-the-art chalcogenides such as CIGS or Sb_2Se_3, this is primarily due to the extremely short research history of $AgBiS_2$. In this regard, we anticipate that our fundamental investigation into the precursor chemistry will provide a key technical foundation for optimizing $AgBiS_2$-based PEC systems.

Conclusion

In this study, we elucidated the relationship between the coordination chemistry of metal cations, ligands (TU), and solvent (DMSO) for the morphology and cation disorder in the final $AgBiS_2$ thin films. We found that the TU–DMSO precursor system is characterized by a strong, inherent structural mismatch between the Ag^+ and Bi^{3+} complexes, specifically a large difference in coordination number and ligand environment. This asymmetry imposes a significant thermodynamic barrier, fundamentally suppressing the formation of a cation-disordered phase in the final $AgBiS_2$ films. Instead, precursor chemistry emerged as a powerful tool for morphology engineering. Systematically increasing the TU/M molar ratio from 1 to 8 facilitated the growth of longer and larger $AgBiS_2$ nanorods. This morphological evolution, driven by the modulated release kinetics of Ag^+ and Bi^{3+} ions, was shown to be the dominant mechanism controlling the structural properties. XRD and XPS analyses confirmed that the observed structural and electronic shifts were consistent with lattice strain relaxation and the resulting reduction in Madelung potential associated with nanorod growth. The potential-induced electronic restructuring resulted in an upward shift of the CBM, creating a more favorable band alignment with the CdS and TiO_2 interlayers. The TU/M = 8 photocathode, featuring optimized nanorod morphology and electronic structure, exhibited a significantly enhanced photocurrent density. Overall, this work establishes that, in TU–DMSO-based $AgBiS_2$ systems, morphology engineering through rational precursor chemistry design represents the primary strategy for optimizing film structure and PEC performance. The molecular-level insights presented here provide a general framework for designing scalable, solution-processed chalcogenide thin films with controlled nanostructure and enhanced device functionality.

Experimental section

Materials

All chemicals were used as received, without additional purifications. Silver chloride powder (AgCl, 99.999%; Sigma-Aldrich), Bismuth(III) chloride powder ($BiCl_3$, 99.99%; Sigma-Aldrich), TU (CH_4N_2S, 99.0%; Sigma-Aldrich), DMSO (C_2H_6OS, 99.7%; Duksan).

Preparation of Ag–Bi–TU–DMSO molecular inks

DMSO solvent was used to dissolve silver chloride, bismuth chloride, and TU to maintain a certain metal to TU molar ratio (1 : 0.5, 1, 2, 4, 8) in a N_2-filled glove box at a metal concentration of 0.2 M for both Ag and Bi solutions. The solutions were stirred for 6 hours, and the fully dissolved solutions are transparent (low TU/M) or yellowish orange (high TU/M).

Fabrication of Au-coated FTO substrates

FTO (TEC 8)-coated substrates were cleaned by sequential sonication with acetone and isopropanol for 15 min each. This was followed by a UV-ozone treatment for 20 min. After cleaning, Au (3 mm Dia × 3 mm Th pellets 4N, iTASCO, Korea) were deposited on cleaned FTO substrates using a thermal evaporator (DDHTSP011, DAEDONG HIGH TECHNOLOGIES, Korea), producing a Au layer of 70 nm. The resulting gold-coated substrates were used in subsequent experiments.

Fabrication of $AgBiS_2$ thin film

Au-coated FTO substrates were cleaned *via* sequential sonication with ethanol, isopropanol (IPA) for 1 min each, followed by UV-ozone treatment for 40 min. The fabrication and annealing of the $AgBiS_2$ thin film were conducted in a N_2-filled glove box. The prepared inks were spin-coated onto the cleaned substrates at various speeds (typically 5000 rpm, adjusted to achieve specific target thicknesses) for 30 s. This process was repeated several times (*e.g.*, four cycles) to achieve the target thickness and morphology. Any specific deviations from these typical parameters (RPM or number of cycles) for individual datasets are specified in the corresponding figure captions. The deposited films were pre-annealed at 200 °C for 5 min after each step, followed by a final post-annealing at 280 °C for 20 min.

Fabrication of $AgBiS_2$ photocathode

CdS layers were deposited *via* chemical bath deposition (CBD) by immersing samples in a bath solution of cadmium sulfate ($CdSO_4$, 99%, Sigma-Aldrich), thiourea (99%, Sigma-Aldrich), deionized water, and ammonium solution (NH_4OH, 25–30 wt%. Duksan, Korea) for 11 min and 30 s at 56.5 °C. Samples were then rinsed using deionized water. TiO_2 layers were deposited *via* customized atomic layer deposition (ALD) using tetrakis(dimethylamino) titanium (TDMAT, Easychem, Korea) and deionized water (H_2O) as the Ti and O sources, respectively. TiO_2 layer was deposited for 750 cycles at 120 °C. An ion sputter coater (G20 ion sputter coater, GSEM, Korea) was used to deposit the Pt co-catalyst for 60 s at a current of 10 mA. For

samples incorporating the TiO_2 interlayer, a layer with a nominal thickness of 1 nm (corresponding to 15 ALD cycles) was deposited prior to CdS deposition. Subsequently, the surface was rendered hydrophilic by UV-ozone treatment for 20 min.

Material characterizations

Raman spectra were recorded using a confocal Raman spectrometer (XperRAM 200, NanoBase, Korea) with a 532 nm excitation laser. Surface morphologies and cross-sectional profiles were analyzed using field-emission scanning electron microscopy (FESEM, JSM-IT800, JEOL Ltd, Japan). Phase identification and evaluation of cation disorder were conducted by high-resolution XRD (Smartlab, Rigaku, Japan) using Cu-Kα radiation (λ = 0.15406 nm). Surface chemical analyses and depth profiles were obtained using XPS (ESCALAB 250Xi, Thermo Scientific, UK). Absorption coefficients were measured using a UV-Vis spectrophotometer (UV-3600i Plus, Shimadzu, Japan). Band structure analyses were performed using ultraviolet photoelectron spectroscopy (NEXSA G2, Thermo Fisher Scientific, USA).

$AgBiS_2$ photocathode performance evaluation

PEC measurements were performed with conventional three-electrode configurations using a potentiostat (PP211, Zahner, Germany) in a 0.5 M K–Pi buffer (pH = 7.02) solution electrolyte. An Ag/AgCl (sat. KCl) and a coiled Pt coil were used as the reference and counter electrodes, respectively. The scan rate of the *J–V* curves was 10 mV s^{-1}. Sunlight simulations and 1-sun calibrations were conducted using a commercial AM 1.5 G solar simulator (LH300, Newport Corporation, USA). Photocurrent density was calculated by dividing the photocurrent by the measured active area of each device. For all PEC measurements, the applied potentials were converted to RHE values using the following equation: $E_{RHE} = E_{Ag/AgCl} + 0.05916\ pH + 0.197$. IPCE measurements were performed using an electrochemical workstation (Zennium, Zahner, Germany) and a potentiostat (PP211, Zahner, Germany) with a monochromatic light source (TLS03, Zahner, Germany).

Computational details

All calculations were performed using the Gaussian 09 software package.[51] Geometry optimization of the ground state and vibrational frequency calculations for Raman spectroscopic analysis were performed at the HF/SDD level of theory, and the energy minima were confirmed by calculations using the zero imaginary modes of vibrations. The binding energy (E_b) between DMSO/TU and Ag^+/Bi^{3+} was calculated from the ground state energies, $E_b = (E_{complex} - E_{ion} - n{*}E_{TU\ or\ DMSO})/m$, where $E_{complex}$ is the total energy of the DMSO–Ag^+, TU–Ag^+, DMSO–Bi^{3+} or TU–Bi^{3+} complex; E_{ion} and $E_{DMSO\ or\ TU}$ denote the energies of the ions (Ag^+ or Bi^{3+}) and DMSO or TU, respectively; and *n* and *m* are the number of DMSO (or TU) molecules and total number of atoms, respectively. All calculations were performed in DMSO using a polarizable continuum model.[52]

Author contributions

D. Lee conceptualized and conducted the overall experiment analysed the data, wrote the manuscript. N. Ha helped experiment and the organization of the initial data. J. Park supervised project and revised the manuscript. J. Jung and J. Lee contributed to data interpretation and discussion. J. H. Kim and S. U. Lee contributed in DFT calculation. D-W. Kang and K. Wang revised manuscript. W. Yang supervised this experiment, directed the research, and contributed to the writing of the manuscript.

Conflicts of interest

There are no conflicts to declare.

Data availability

Data are available upon reasonable request from the authors.

Supplementary information (SI) is available. See DOI: https://doi.org/10.1039/d6ta01212d.

Acknowledgements

This work was supported by the National R&D Program of the National Research Foundation of Korea (NRF), funded by the Ministry of Science and ICT (Grant no RS-2025-05482972 and RS-2025-24492969).

Notes and references

1 W. Yang, R. R. Prabhakar, J. Tan, S. D. Tilley and J. Moon, *Chem. Soc. Rev.*, 2019, **48**, 4979–5015.
2 R. Devika, P. Vengatesh and T. Shyju, *Mater. Today Proc.*, 2023, **15**, 21541–21554.
3 S. Hadke, M. Huang, C. Chen, Y. F. Tay, S. Chen, J. Tang and L. Wong, *Chem. Rev.*, 2021, **122**, 10170–10265.
4 E. Gu, X. Lin, X. Tang, G. J. Matt, A. Osvet, Y. Hou, S. Jäger, C. Xie, A. Karl and R. Hock, *J. Mater. Chem. C*, 2018, **6**, 7642–7651.
5 Y. Wu, L. Wan, W. Zhang, X. Li and J. Fang, *CrystEngComm*, 2019, **21**, 3137–3141.
6 J. van Embden and E. Della Gaspera, *ACS Appl. Mater. Interfaces*, 2019, **11**, 16674–16682.
7 N. Ha, J. Jung, D. Lee, J. Park, H. Shin, S. U. Lee and W. Yang, *J. Mater. Chem. A*, 2026, **14**, 2167–2178.
8 N. Ha, G. Lee, J. Park, J. H. Lee, J. Jung, S. V. Barma, J. Kim, J. H. Kim, J. K. Kim and S. J. Kwon, *Adv. Energy Mater.*, 2025, **15**, 2402099.
9 Y. Wang, S. R. Kavanagh, I. Burgués-Ceballos, A. Walsh, D. O. Scanlon and G. Konstantatos, *Nat. Photonics*, 2022, **16**, 235–241.
10 M. Righetto, Y. Wang, K. A. Elmestekawy, C. Q. Xia, M. B. Johnston, G. Konstantatos and L. M. Herz, *Adv. Mater.*, 2023, **35**, 2305009.
11 M. Bernechea, N. Cates, G. Xercavins, D. So, A. Stavrinadis and G. Konstantatos, *Nat. Photonics*, 2016, **10**, 521–525.

12 J. Jung, N. Ha and W. Yang, *ACS Appl. Mater. Interfaces*, 2025, **17**, 16410–16420.
13 J. Cen, B. Zhu, S. R. Kavanagh, A. G. Squires and D. O. Scanlon, *J. Mater. Chem. A*, 2023, **11**, 13353–13370.
14 X. Ou, T. Liu, W. Zhong, X. Fan, X. Guo, X. Huang, L. Cao, J. Hu, B. Zhang and Y. S. Chu, *Nat. Commun.*, 2022, **13**, 2319.
15 D. Bosubabu, P. M. Ette, A. K. Nanda Kumar, A. Arulraj and K. Ramesha, *ACS Appl. Energy Mater.*, 2020, **3**, 8716–8724.
16 C. Malerba, M. Valentini and A. Mittiga, *Sol. RRL*, 2017, **1**, 1700101.
17 C. Bosson, M. Birch, D. Halliday, K. Knight, A. Gibbs and P. Hatton, *J. Mater. Chem. A*, 2017, **5**, 16672–16680.
18 J. Qu, A. Elgendy, R. Cai, M. A. Buckingham, A. A. Papaderakis, H. De Latour, K. Hazeldine, G. F. Whitehead, F. Alam and C. T. Smith, *Adv. Sci.*, 2023, **10**, 2204488.
19 Y.-T. Huang, S. R. Kavanagh, M. Righetto, M. Rusu, I. Levine, T. Unold, S. J. Zelewski, A. J. Sneyd, K. Zhang and L. Dai, *Nat. Commun.*, 2022, **13**, 4960.
20 J. Tan, X. Zhang, J. Suh, N. Ha, J. Lee, S. D. Tilley and W. Yang, *Mater. Today Energy*, 2023, **34**, 101288.
21 W. Yang, J. Ahn, Y. Oh, J. Tan, H. Lee, J. Park, H. C. Kwon, J. Kim, W. Jo and J. Kim, *Adv. Energy Mater.*, 2018, **8**, 1702888.
22 A. Kontos, A. Kontos, D. Tsoukleris, V. Likodimos, J. Kunze, P. Schmuki and P. Falaras, *Nanotechnology*, 2008, **20**, 045603.
23 D. Sengupta, P. Das, B. Mondal and K. Mukherjee, *Renewable Sustainable Energy Rev.*, 2016, **60**, 356–376.
24 E. Thimsen, N. Rastgar and P. Biswas, *J. Phys. Chem. C*, 2008, **112**, 4134–4140.
25 J. Joo, T. Kim, J. Lee, S. I. Choi and K. Lee, *Adv. Mater.*, 2019, **31**, 1806682.
26 K. Lan, J. Li, Y. Zhu, L. Gong, F. Li, P. Jiang, F. Niu and R. Li, *J. Colloid Interface Sci.*, 2019, **539**, 646–653.
27 E. Samuel, B. Joshi, M.-W. Kim, M. T. Swihart and S. S. Yoon, *Nano Energy*, 2020, **72**, 104648.
28 J. Park, K.-Y. Yoon, B. G. Ghule, H. Kim and J.-H. Jang, *ACS Energy Lett.*, 2024, **9**, 3169–3176.
29 X. Yang, H. Xiang, J. Huang, C. Zhou, R. Ran, W. Wang, W. Zhou and Z. Shao, *J. Colloid Interface Sci.*, 2022, **628**, 476–485.
30 Z. Li, G. Zhang, Z. Li, Y. Xie, Y. Xia, Z. Hu, L. Chao, F. Wang and Y. Chen, *CrystEngComm*, 2024, **26**, 3026–3032.
31 H.-J. Zhai and H.-S. Wang, *Mater. Res. Bull.*, 2008, **43**, 2354–2360.
32 W. Yang, Y. Oh, J. Kim, M. J. Jeong, J. H. Park and J. Moon, *ACS Energy Lett.*, 2016, **1**, 1127–1136.
33 A. Tofoni, M. Busato, A. Colella, A. Melchior and P. D'Angelo, *J. Phys. Chem. B*, 2024, **128**, 8065–8073.
34 J. C. Xiang, Q. H. Gao and A. X. Wu, in *Solvents as Reagents in Organic Synthesis: Reactions, Applications*, ed. X.-F. Wu, Wiley-VCH, Weinheim, 2017, ch. 7, pp. 315–353.
35 A. Uhl, J. Katahara and H. Hillhouse, *Energy Environ. Sci.*, 2016, **9**, 130–134.
36 H. Xin, J. K. Katahara, I. L. Braly and H. W. Hillhouse, *Adv. Energy Mater.*, 2014, **4**, 1301823.
37 S. Engberg, F. Martinho, M. Gansukh, A. Protti, R. Küngas, E. Stamate, O. Hansen, S. Canulescu and J. Schou, *Sci. Rep.*, 2020, **10**, 20749.
38 T. K. Chaudhuri, M. H. Patel, D. Tiwari and P. R. Ghediya, *J. Alloys Compd.*, 2018, **747**, 31–37.
39 J. A. Clark, A. R. Uhl, T. R. Martin and H. W. Hillhouse, *Chem. Mater.*, 2017, **29**, 9328–9339.
40 V. Trifiletti, S. Mostoni, F. Butrichi, M. Acciarri, S. Binetti and R. Scotti, *ChemistrySelect*, 2019, **4**, 4905–4912.
41 B. Zhang, Y. Yu, Z. Wang and J. Zhang, *Appl. Surf. Sci.*, 2010, **256**, 6506–6511.
42 S. Moon, J. Park, H. Lee, J. W. Yang, J. Yun, Y. S. Park, J. Lee, H. Im, H. W. Jang and W. Yang, *Adv. Sci.*, 2023, **10**, 2206286.
43 J. Wang, L. Li, H. Yu, F. Guan and D. Wang, *Inorg. Chem.*, 2019, **58**, 12998–13006.
44 Y. Yu, C. Jin, R. Wang, Q. Chen and L.-M. Peng, *J. Phys. Chem. B*, 2005, **109**, 18772–18776.
45 M. Sharma, K. K. Mishra, S. Singh, S. K. Singh and P. Singh, *Int. J. Hydrogen Energy*, 2025, **132**, 116–129.
46 G. Greczynski, R. T. Haasch, N. Hellgren, E. Lewin and L. Hultman, *Nat. Rev. Methods Primers*, 2023, **3**, 40.
47 C. Zhou, Z. Xi, D. J. Stacchiola and M. Liu, *Energy Sci. Eng.*, 2022, **10**, 1614–1629.
48 S. Xie, X. Li, Q. Lai, W. Wang and G. Li, *Small*, 2026, **22**, e10969.
49 J. Lin, Y. Yu, Z. Zhang, F. Gao, S. Liu, W. Wang and G. Li, *Adv. Funct. Mater.*, 2020, **30**, 1910479.
50 M.-G. Ju, J. Dai, L. Ma, Y. Zhou and X. C. Zeng, *Nanoscale Adv.*, 2020, **2**, 770–776.
51 M. Frisch, G. Trucks, H. Schlegel, G. Scuseria, M. Robb, J. Cheeseman, G. Scalmani, V. Barone, B. Mennucci and G. Petersson, *Gaussian 09, Revision D. 01*, Gaussian, Inc, Wallingford, CT 2013.
52 M. Cossi, N. Rega, G. Scalmani and V. Barone, *J. Comput. Chem.*, 2003, **24**, 669.
53 T. Shinagawa and K. Takanabe, *ChemSusChem*, 2017, **10**, 1318–1336.